UC Santa Cruz
UC Santa Cruz Previously Published Works

Title

The Carousel Lens: A Well-modeled Strong Lens with Multiple Sources Spectroscopically Confirmed by VLT/MUSE

Permalink

Journal

ISSN

Authors

Sheu, William
Cikota, Aleksandar
Huang, Xiaosheng
et al.

Publication Date

DOI

Copyright Information

The Carousel Lens: A Well-Modeled Strong Lens with Multiple Sources Spectroscopically Confirmed by VLT/MUSE

William Sheu [ID],[1] Aleksandar Cikota [ID],[2] Xiaosheng Huang [ID],[3, 4] Karl Glazebrook [ID],[5, 6]
Christopher Storfer [ID],[4, 7] Shrihan Agarwal [ID],[8] David J. Schlegel [ID],[4] Nao Suzuki [ID],[4, 9, 10]
Tania M. Barone [ID],[5, 6] Fuyan Bian [ID],[11] Tesla Jeltema [ID],[12] Tucker Jones [ID],[13] Glenn G. Kacprzak [ID],[5, 6]
Jackson H. O'Donnell [ID],[12] and Keerthi Vasan G. C. [ID][13]

[1]Department of Physics & Astronomy, University of California, Los Angeles, 430 Portola Plaza, Los Angeles, CA 90095, USA
[2]Gemini Observatory / NSF's NOIRLab, Casilla 603, La Serena, Chile
[3]Department of Physics & Astronomy, University of San Francisco, 2130 Fulton Street, San Francisco, CA 94117-1080, USA
[4]Physics Division, Lawrence Berkeley National Laboratory, 1 Cyclotron Road, Berkeley, CA 94720, USA
[5]Centre for Astrophysics and Supercomputing, Swinburne University of Technology, Hawthorn, Victoria 3122, Australia
[6]ARC Centre of Excellence for All Sky Astrophysics in 3 Dimensions (ASTRO 3D), Australia
[7]Institute for Astronomy, University of Hawaii, 2680 Woodlawn Drive, Honolulu, HI 96822-1897, USA
[8]Department of Astronomy, University of Chicago, 5640 S Ellis Ave, Chicago, IL 60615, USA
[9]Department of Physics, Florida State University, 77 Chieftan Way, Tallahassee, FL 32306, USA
[10]Kavli Institute for the Physics and Mathematics of the Universe, University of Tokyo, Kashiwa 277-8583, Japan
[11]European Southern Observatory, Alonso de Córdova 3107, Casilla 19001, Vitacura, Santiago 19, Chile
[12]Santa Cruz Institute for Particle Physics, Santa Cruz, CA 95064, USA
[13]Department of Physics and Astronomy, University of California, Davis, 1 Shields Avenue, Davis, CA 95616, USA

ABSTRACT

Over the past few years alone, the lensing community has discovered thousands of strong lens candidates, and spectroscopically confirmed hundreds of them. In this time of abundance, it becomes pragmatic to focus our time and resources on the few extraordinary systems, in order to most efficiently study the universe. In this paper, we present such a system: DESI-090.9854-35.9683, a cluster-scale lens at $z_l = 0.49$, with seven observed lensed sources around the core, and additional lensed sources further out in the cluster. From the number and the textbook configuration of the lensed images, a tight constraint on the mass potential of the lens is possible. This would allow for detailed analysis on the dark and luminous matter content within galaxy clusters, as well as a probe into dark energy and high-redshift galaxies. We present our spatially resolved kinematic measurements of this system from the Very Large Telescope Multi Unit Spectroscopic Explorer, which confirm five of these source galaxies (in ascending order, at $z_s = 0.962, 0.962, 1.166, 1.432,$ and 1.432). With previous *Hubble Space Telescope* imaging in the F140W and F200LP bands, we also present a simple two power-law profile flux-based lens model that, for a cluster lens, well models the five lensed arc families with redshifts. We determine the mass to be $M(< \theta_E) = 4.78 \times 10^{13} M_\odot$ for the primary mass potential. From the model, we extrapolate the redshift of one of the two source galaxies not yet spectroscopically confirmed to be at $z_s = 4.52^{+1.03}_{-0.71}$.

Keywords: Strong gravitational lensing — Galaxy clusters — Galaxy spectroscopy — High-redshift galaxies

1. INTRODUCTION

Corresponding author: William Sheu
wsheu@astro.ucla.edu
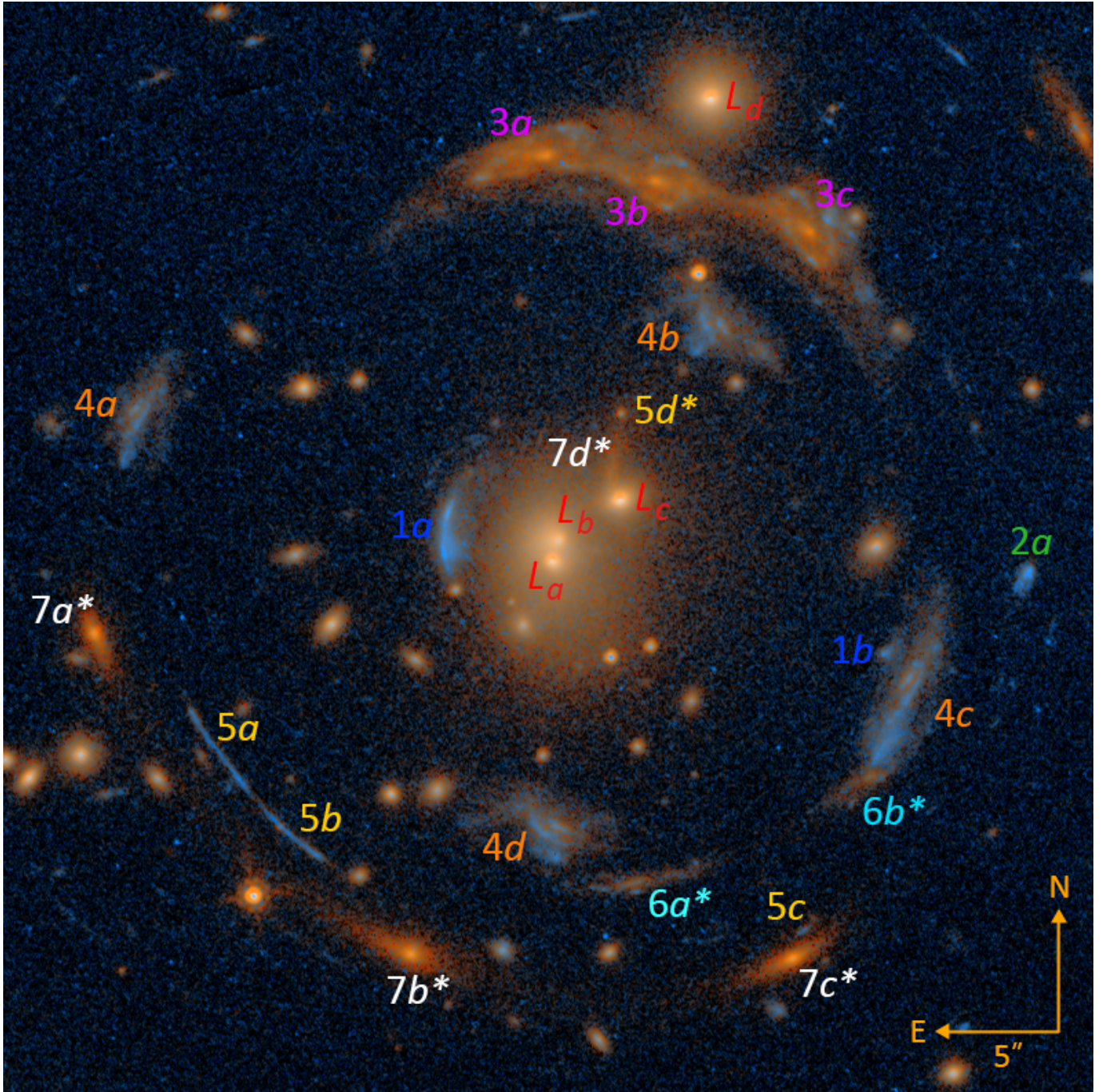
Figure 1. RGB image of DESI-090.9854-35.9683, generated using the *HST* F140W filter ($0.070''$/pixel) as the red channel, *HST* F200LP filter ($0.028''$/pixel) as the blue channel, and the pixel-wise average of the two filters as the green channel. The brightest cluster-member galaxies within our cutout, labeled as L_a, L_b, L_c, and L_d, are approximately at the same redshift of $z_l = 0.49$ (see Table 1). The source galaxy images, labeled with a number prefix and a letter, are organized such that images of the same numeral prefix and color correspond to the same source galaxy. Note that $2a$ is the only image for this arc family. Image labels followed by an asterisk indicate that they do not exhibit prominent lines in the MUSE IFU data, and hence we cannot spectroscopically confirm their redshifts. The spectroscopic redshifts of galaxies 1, 2, 3, 4, and 5 are $z_s = 0.962, 0.962, 1.166, 1.432,$ and 1.432, respectively (see §3).

Strong lensing occurs when the gravity of a massive object, typically a galaxy or galaxy cluster, distorts the light path from a background source galaxy with near perfect alignment with the observer. These distortions can result in multiple, magnified, and warped images of the source galaxy surrounding the lensing object. These systems are invaluable probes to many facets of cosmology. By fitting for the lensed images and analyzing the lens galaxy kinematics, we can study the dark matter profiles of the lens (e.g., Shajib et al. 2021). By measuring and modeling the time delays of lensed transient events or variable objects between the multiple images, we can constrain the Hubble constant H_0, independent of the CMB and direct distance ladder measurements, which currently disagree (e.g., Wong et al. 2020). By virtue of its ability to drastically magnify background sources, strong lensing allows for significantly deeper and further observations than otherwise possible (e.g., Roberts-Borsani et al. 2022).

This paper is organized as follows: we describe the general properties and discovery status of DESI-090.9854-35.9683 (§2), provide our analysis of the Multi Unit Spectroscopic Explorer (MUSE) integral field units (IFU) data (§3), present our lens model of the system (§4), discuss the possible redshift of one of the lensed sources (§5), and conclude (§6).

2. DESI-090.9854-35.9683 DISCOVERY AND PROPERTIES

DESI-090.9854-35.9683 (RA: $6^h3^m56{\overset{s}{.}}50$, dec.: $-35°58'5{\overset{''}{.}}88$) was first identified in Jacobs et al. (2019) as a "possible, but not probable or definite" strong lens system candidate by applying a convolutional neural network to the Dark Energy Survey (DES) Year 3 imaging. Its low score is likely due to the small cutouts ($26'' \times 26''$) used during visual inspection, which missed the large cluster-scale lensing nature (Jacobs et al. 2019). Huang et al. (2021) later independently identified this system with a residual neural network on the Dark Energy Spectroscopic Instrument (DESI) Legacy Imaging Surveys Data Release 8; following visual human inspection, the system was given a strong lens candidacy grade of A (see their Figure 10). This system was also found by O'Donnell et al. (2022) as DESJ0603-3558, by applying a color-magnitude selection to catalogs created from the first three observing seasons of DES, followed by visual scanning. DESI-090.9854-35.9683 was observed by the *Hubble Space Telescope* (*HST*) Wide Field Camera 3 for 600 seconds each in the F140W and F200LP filters (*HST* proposal #16773; K. Glazebrook), which is shown as an RGB image in Figure 1. All the *HST* data used in this paper can be obtained from the MAST archive at 10.17909/zq07-4f53. Throughout this paper, we will reference the labeling scheme illustrated in Figure 1.

Strong lensing in DESI-090.9854-35.9683 occurs around the center of a small cluster with four spectroscopically confirmed source galaxies, plus one weakly lensed galaxy. While this is a cluster lens, we note that the lens profile does not seem overly complex, as the lensed image configurations for arc families 1, 3, 4, and 7 are typical of simple lens profiles, implying a fairly relaxed lensing potential. Source galaxy 1 ($z_s = 0.962$; see §3) is doubly lensed. Source galaxy 2 ($z_s = 0.962$) appears to have only one lensed image, and hence is weakly lensed. The lensed images of source galaxy 3 ($z_s = 1.166$) appear to be in a "naked cusp" configuration (e.g., Bradač et al. 2004), given that there are three bright images merging, and yet a fourth image is not present in the MUSE data cube nor in our model predictions. Such a configuration is only possible if the lens' inner diamond caustic extends outside its elliptical caustic, which gives additional insight on the lens potential (e.g., Narayan & Wallington 1992; Kochanek 1992). Also, the source galaxy 3 images are significantly perturbed by one of the cluster member galaxies L_d, in addition to the main cluster profile centered near galaxies L_a, L_b, and L_c. Source galaxy 4 ($z_s = 1.432$) is quadruply lensed in an Einstein cross configuration; this source exhibits a high level of structural complexity. Source galaxy 5 ($z_s = 1.432$) appears to be quadruply lensed, with a demagnified fourth image 5d predicted by our model (see §4). Given the similarity in their colors, morphology, and their tangential elongation, we posit that objects 6a and 6b are lensed images of the same source galaxy, but no spectroscopic redshift can be identified from the MUSE data (though the MUSE data cube does indeed distinguish object 6b from 4c). Source galaxy 7 is quadruply lensed, with 7d being a radial arc. Not only is the color of 7d consistent with $7a - 7c$, but the location is in agreement with lens modeling (see §5). There are no prominent spectroscopic lines present for source galaxy 7 in the MUSE observations, but our lens modeling predicts a redshift of $z_s = 4.52^{+1.03}_{-0.71}$ (also in §5), which would make it an interesting probe into high-redshift galaxies.

In addition to its prominent lensing features, DESI-090.9854-35.9683 was also identified as a Sunyaev-Zel'dovich (SZ) galaxy cluster through X-ray detections in the ROSAT All-Sky Survey (Voges et al. 2000; Flesch 2010; Tarrío et al. 2019), and microwave detections from the Atacama Cosmology Telescope (Hilton et al. 2021).

3. MUSE IFU OBSERVATIONS

DESI-090.9854-35.9683 was observed on September 30, 2023 at 07:45h UT (Prog. ID 0111.B-0400(H)) with MUSE (Bacon et al. 2010), an IFU spectrograph mounted at UT4 of ESO's Very Large Telescope (VLT) on Cerro Paranal in

Table 1. Lens and source redshifts, and their statistical uncertainties. The redshifts have been determined by fitting the Ca H&K line in the case of the L_{a+b}, L_c and L_d, or the [O II] doublet in the case of the lensed images of the sources ($1a - 5b$). The proper velocity difference is calculated as $v_i = c(z_i - z)/(1 + z)$, where z is the average of the images redshifts for each source (or the average of the cluster-member galaxy redshifts in the case of L_{a+b}, L_b, and L_c). The proper velocity for $2a$ is calculated assuming it is of the same source as $1a$ and $1b$, resulting in the outlying velocity presented.

Object	Redshift	Proper velocity difference
		[km s^{-1}]
L_{a+b}	0.48784 ± 0.00045	-123.5 ± 98.8
L_c	0.48716 ± 0.00033	-260.5 ± 77.4
L_d	0.49036 ± 0.00019	384.0 ± 55.1
$1a$	0.96196 ± 0.00001	25.0 ± 4.2
$1b$	0.96189 ± 0.00007	14.3 ± 11.4
$2a$	0.96154 ± 0.00003	-39.2 ± 6.0
$3a$	1.1657 ± 0.0001	-38.6 ± 17.9
$3b$	1.1659 ± 0.0002	-19.4 ± 29.9
$3c$	1.1664 ± 0.0001	58.1 ± 17.8
$4a$	1.43227 ± 0.00003	-4.9 ± 4.0
$4b$	1.43230 ± 0.00002	-1.2 ± 2.8
$4c$	1.43233 ± 0.00002	2.5 ± 2.8
$4d$	1.43234 ± 0.00002	3.7 ± 2.8
$5a$	1.43198 ± 0.00004	-1.9 ± 5.8
$5b$	1.43201 ± 0.00003	1.9 ± 4.8

Chile. The observations were carried out in the MUSE WFM-NOAO-N mode, with a field of view of $60'' \times 60''$ and a spaxel size of $0.2''$. The spectral range is from 4750 to 9350 Å with the spectral resolution ranging from R = 2000 to 4000 Å across the wavelength domain. The observations were taken with 4×700 second exposures during DIMM seeing of $\sim 0.9''$ in clear but windy (~ 10 m/s) weather, and reduced following standard procedures with the MUSE pipeline package version 2.2 (Weilbacher et al. 2020) that is a part of the ESO Recipe Execution Tool (ESOREX). We also removed sky lines using the Zurich Atmosphere Purge (ZAP) sky subtraction tool (Soto et al. 2016).

We extracted the spectra of the lens and the lensed images of the sources from the MUSE data cube and determined the redshifts by matching prominent emission and absorption lines to the spectra (Figure 2). Using the Ca H&K lines, we successfully determine the redshifts of the lensing galaxies ($L_a + L_b$, see Figure 1 for a map of objects), which also display prominent G band, Mg b, and Na I D absorption lines, and of the lensed images of source galaxies 1, 2, 3, 4, and 5 on account of the [O II] $\lambda\lambda$ 3726.1, 3728.8 doublet. All redshifts are given in Table 1. The lensing galaxies, L_{a+b}, are part of a galaxy cluster. The other two bright members, L_c and L_d, also display prominent absorption lines at a redshift consistent with proper velocities within galaxy clusters. From these three measurements, we calculate a mean cluster redshift of $z = 0.4884 \pm 0.0014$. We also note that the source galaxies 1 and 2 have similar redshifts of $z_s = 0.962$, and source galaxies 4 and 5 have similar redshifts of $z_s = 1.432$. This may indicate that we are observing

a series of three galaxy groups/clusters that lie on the same line-of-sight. Lastly, source galaxy 3 has a redshift of $z_s = 1.166$.

The lensed galaxy 1 displays 2 arcs, $1a$ and $1b$ at consistent redshifts (see Figure 2). Initially, the bright image 2 was thought to be the counterarc of $1a$; however, lens modeling (see §4) showed inconsistencies with the expected position of the image $1b$. Furthermore, the redshift of $2a$ is also inconsistent with the redshift of $1a$ (with a 6.3σ discrepancy; see Figure 2 and Table 1). Figure 3 shows a proper velocity difference map of the images, and it is clear that, while all the other images have consistent velocities, the velocity of source 2 is an outlier. A closer inspection of the MUSE cube reveled a faint counterarc, $1b$, at the expected position. We conclude that image $2a$ belongs to a singly lensed galaxy distinct from arc family 1. In image $1a$, the [O III] is detected, which could be used to probe the gas-phase metallicity of source galaxy 1 in future analysis.

Source galaxy 3 displays three lensed images north of the lens: $3a$, $3b$, and $3c$, at a redshift of $z_s = 1.166$. In Table 1, we see significant differences in the proper velocity between images $3a$, $3b$, and $3c$, which we associate as being due to their diffused imaging in the MUSE cube (see Figure 3). Because of this, we cannot well ascertain which part of the source galaxy we are probing through the spectra of each image. Therefore, the significant difference in proper velocities are likely due to rotation/dispersion within the source galaxy, and our spaxel selection capturing different regions of the source galaxy for each image.

The source galaxies 4 and 5 are both quadruply lensed and at a similar redshift of $z_s = 1.432$. The quad lensed images of source galaxy 4 exhibit textbook parities (see right panel of Figure 3), indicating that the central part of the cluster is dynamically relaxed. This, together with the overall relatively high degree of symmetry of this system, motivated a relatively simple lens model in the next section. Although their redshifts are similar, there is a statistically significant difference between source 4 and 5 (of 6.2σ; see Table 1). Source galaxy 5 displays two bright arcs, clearly visible in the MUSE data (see left panel in Figure 3), $5a$ and $5b$. The position of image $5c$ is predicted by the lens model and found in the MUSE datacube after closer examination. The image $5c$ is faint, and so we do not show its spectrum in Figure 2, but the [O II] emission is visible in the line-map (see left panel in Figure 3). $5d$ is also predicted by the lens model, but as it is demagnified and therefore even fainter, it cannot be spectroscopically confirmed by the MUSE data.

The images of source galaxy 6 are visible in the Near-IR *HST* images, but very faint in the *HST* optical F200LP filter, and are not visible in the MUSE (optical) data. The images of source 7 (Figure 6) are faint, but visible in the collapsed MUSE image. However the extracted spectra do not show any prominent lines, and so we can not determine the redshift (see more about source galaxy 7 in §5).

In the spectra for source galaxies $1 - 5$ (Figure 2), the [O II] doublet is well resolved. Not only does this allow for accurate redshift measurements (as shown in this paper), but it can also be used to probe the densities of these source galaxies. We leave the detailed spectral analysis for future works. Though we do not yet have spectroscopic redshifts for arc families 6 and 7 ($6a$, b and $7a$, b, c, respectively), based on the *HST* observations (Figure 1), it is clear that they are lensed arcs: 1) by the arrangement of images in these two arc families, namely, they form an arc with the center of curvature matching the center of the cluster; and 2) by the similarity in morphology and color for images $6a$ and $6b$, and for images $7a$, b and c, respectively. More quantitatively for images $7a$, b, and c, Table 3 shows that they have very similarly SEDs.

4. LENS MODELING

We use LENSTRONOMY[1], a multi-purpose lens modeling software package, to model DESI-090.9854-35.9683, with multiple source redshift planes to account for each source galaxy (Birrer & Amara 2018; Birrer et al. 2021). LENSTRONOMY implements a forward-modeling algorithm to estimate the lens potential and surface brightness profiles, by reconstructing an image of the lensing system and minimizing over the pixel-level residuals with the data. In the Time-Delay Lens Modeling Challenge (TDLMC; Ding et al. 2021), LENSTRONOMY has proved robust and accurate, it was used by multiple teams to recover lens model parameters within statistical consistency (in Rung 2).

In this paper, we model based on the F140W image as opposed to the F200LP, as the SNR in source galaxies 3 and 4 are clearly higher in the F140W filter. Our model consists of two elliptical power law lens profiles (both at $z_l = 0.49$), centered at object L_a and L_d respectively. This was the best model (compared to other iterations of power law lenses centered at L_a, L_b, L_c, and L_d) based on the lowest Bayesian information criterion (BIC) value using solely lensed

---

[1] https://github.com/lenstronomy/lenstronomy
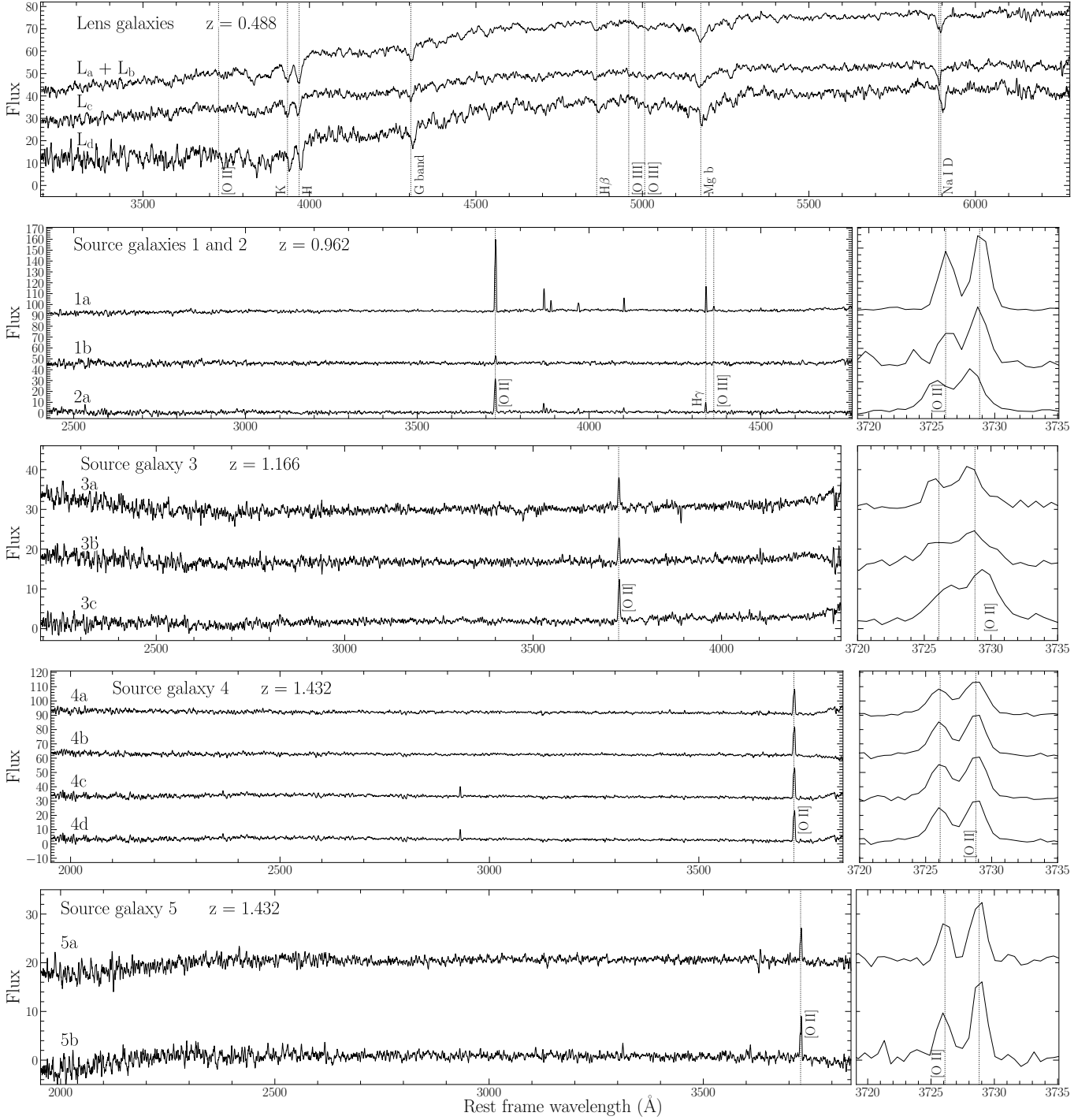
Figure 2. Spectra of the lens and images of the sources extracted from the MUSE cube. The spectra are the average of multiple hand-selected spaxels for each object (see Figure 3). The right panels for the sources are cut-outs around the [O II] $\lambda\lambda$ 3726.1, 3728.8 doublet line used for the redshift determination.

image positions. As objects L_a, L_b, L_c, and L_d are the brightest cluster members in the cutout, their light profiles are modeled with elliptical Sérsic profiles (Sérsic 1963) so as to prevent their lens light from contaminating the lensed images. All other interloping objects, as well as source galaxy 6 and 7 images (since we do not have spectroscopic redshifts for these), are masked out (see the top right panel of Figure 4). The light profiles for source galaxies 1, 3,
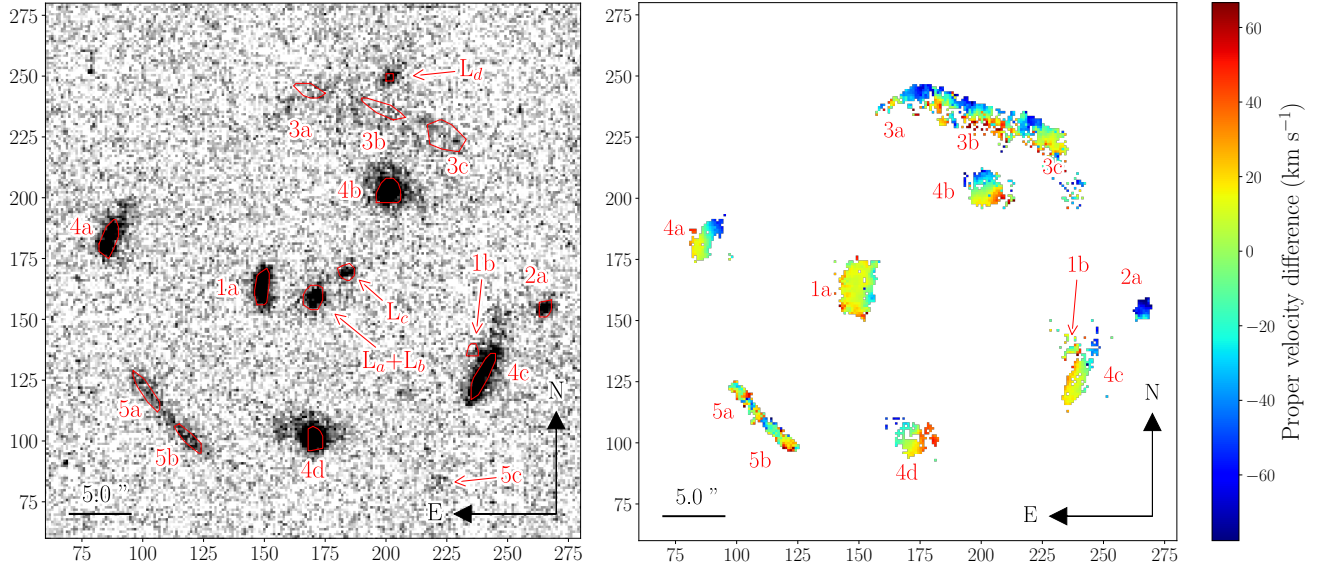
Figure 3. Cutouts of the MUSE data of DESI-090.9854-35.9683. The scale is in pixels, where the pixel size is $0.2''$. North is up, east left. Left: the [O II]$\lambda\lambda$ 3726.1, 3728.8 line-map of the images 1, 2, 3, 4, and 5. The red outlines illustrate the spaxels used in generating the spectra in Figure 2. Right: the proper velocity map of the lensed images. The velocity difference is relative to the average redshift for each respective source.

Table 2. Lens model parameters and their statistical uncertainties. Here, $\theta_{\rm E}$ is the Einstein radius (with respect to $z_{\rm s} = 1.432$), γ is the the logarithmic slope of the mass profile, q is the mass axis ratio, PA is the mass position angle, $M(< \theta_{\rm E})$ is the projected mass within the Einstein radius, $\gamma^{\rm ext}$ is the external shear magnitude, and $\phi^{\rm ext}$ is the external shear angle. All angular measures are given as North of East.

Object	$\theta_{\rm E}$	γ	q	PA	$M(< \theta_{\rm E})$	$\gamma^{\rm ext}$	$\phi^{\rm ext}$
	['']			[deg]	$[10^{11} M_\odot]$		[deg]
L_a	13.03 ± 0.02	1.67 ± 0.01	0.87 ± 0.01	-45 ± 1	478 ± 2	-	-
L_d	0.99 ± 0.02	2.12 ± 0.01	0.69 ± 0.01	-38 ± 1	2.77 ± 0.12	-	-
External Shear	-	-	-	-	-	0.11 ± 0.01	9 ± 1

4, and 5 are each modeled with an elliptical Sérsic profile and a shapelets basis (Refregier 2003; Refregier & Bacon 2003; Birrer et al. 2015) of order 10, 15, 9, and 8, respectively. These orders are determined through trial and error to improve the model fit with the best reduced χ^2 (e.g., Tan et al. 2024). A Bayesian model comparison is often used to assess and determine how a given model fits the image data (e.g., Nightingale et al. 2018; Shajib et al. 2018), but given the number of sources and the permutations of orders, this method would be computationally impractical. For source galaxy 2, we only implement a single elliptical Sérsic profile, as there is only one image present, and its appearance does not necessitate additional complexity. We note that while source 2 (being singly imaged) does not contribute as much constraining power to model as compared to the other lensed sources, the fact that it is singly imaged narrows the lensing parameter space by forcing the delensed image to lie outside the caustic. While it can be argued that this parameter space is already being excluded by the other image constraints, we nevertheless include source 2 into our model as further confirmation. We model the point spread function (PSF) by stacking nearby stars in the *HST* exposure[2].

---

[2] We apply the implementation provided in https://github.com/sibirrer/AstroObjectAnalyser.
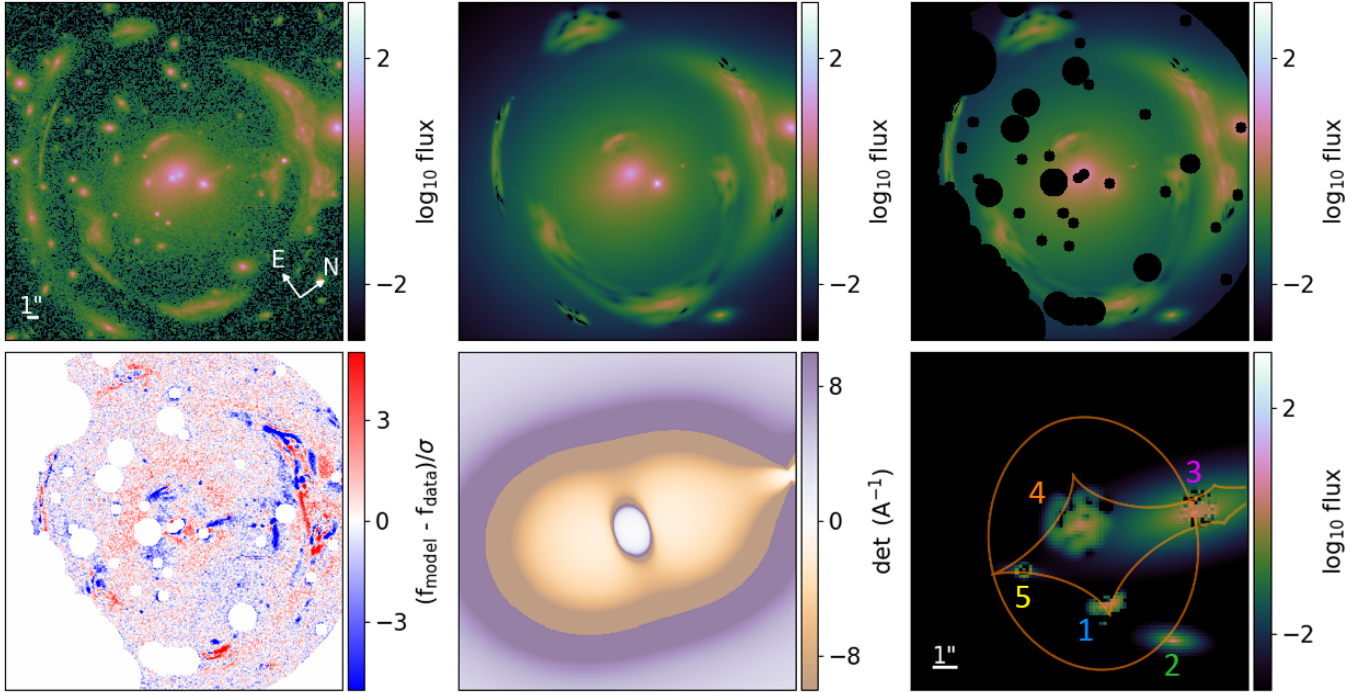
Figure 4. Modeling results for DESI-090.9854-35.9683. Top left: the *HST* F140W image. Top middle: the resulting best-fitting model. Top right: the best-fitting model, with the masks used in the modeling process. Bottom left: the normalized residuals. Bottom middle: the magnification map at the lens plane assuming $z_s = 1.432$. Bottom right: the source plane image, overlaid with the caustic at $z_s = 1.432$, and labels corresponding to the source galaxies. All panels but the source plane panel (bottom right) share the same compass and scale bar as the data panel (top left).

We then fit our model to the data, with first a particle swarm optimization operation to locate a maximum (likely close to the global) of the lens likelihood function, then a Markov chain Monte Carlo (MCMC) algorithm with EMCEE to probe the statistical uncertainties of our model parameters (Foreman-Mackey et al. 2013). The model and its residuals are shown in Figure 4, our parameterizations and statistical uncertainties in Table 2, and the model posteriors are presented in Figure 5. Additionally, we show our model's predicted lensed image locations over the *HST* F140W image in Figure 6. We accomplish this by finding the lensed positions of the shapelets source light profile centers for galaxies 1, 3, 4, and 5 (since the shapelets light contribution exhibits a higher peak flux than their Sérsic counterpart); we use the Sérsic profile center for galaxy 2 as we do not model a shapelets profile for it.

The model achieves a reduced χ^2 of 2.3. For the primary lensing power-law profile, we find the best-fit Einstein radius to be $\theta_E = 13.03'' \pm 0.02$ (using $z_s = 1.432$) and the power-law slope, $\gamma = 1.67 \pm 0.01$ (corresponding to a total two-dimensional projected mass within the Einstein radius of $4.78 \times 10^{13} M_\odot$). This is significantly steeper ($\sim 3\sigma$) than population-level total densities of galaxy clusters at $z = 0.2 - 0.3$ (Newman et al. 2013), but could be explained by our model systematics (as discussed in the paragraph after next), and/or galaxy cluster density profile evolution (Mostoghiu et al. 2019).

Through the trial-and-error of our modeling process, we made several revelations that helped us in identifying the source images. We had initially thought image $2a$ to be the counterarc of image $1a$ due to their similar redshifts ($z_s = 0.96196$ for $1a$ and $z_s = 0.96154$ for $2a$; see Table 1), relative locations, and similar colors. However, from inconsistencies with our predicted counterarc location, we correctly found image $1b$ to be the counter image and $2a$ as a separate lensed galaxy (which is now spectroscopically confirmed; see Table 1). Additionally, through constraining images $5a$ and $5b$, our model placed source galaxy 5 to lie just inside the caustic, predicting two additional images near $5c$ and $5d$ (commonly referred to as a "fold" configuration). After re-examining the MUSE data, we confirmed $5c$ to indeed be a lensed image, though $5d$ remains to be too dim to resolve its spectra.

Note that the modeling uncertainties presented in this paper are only statistical. For example, our relatively simple model assumes that the primary lens has a uniform γ. From N-body simulation for CDM (e.g., Navarro et al. 1996),
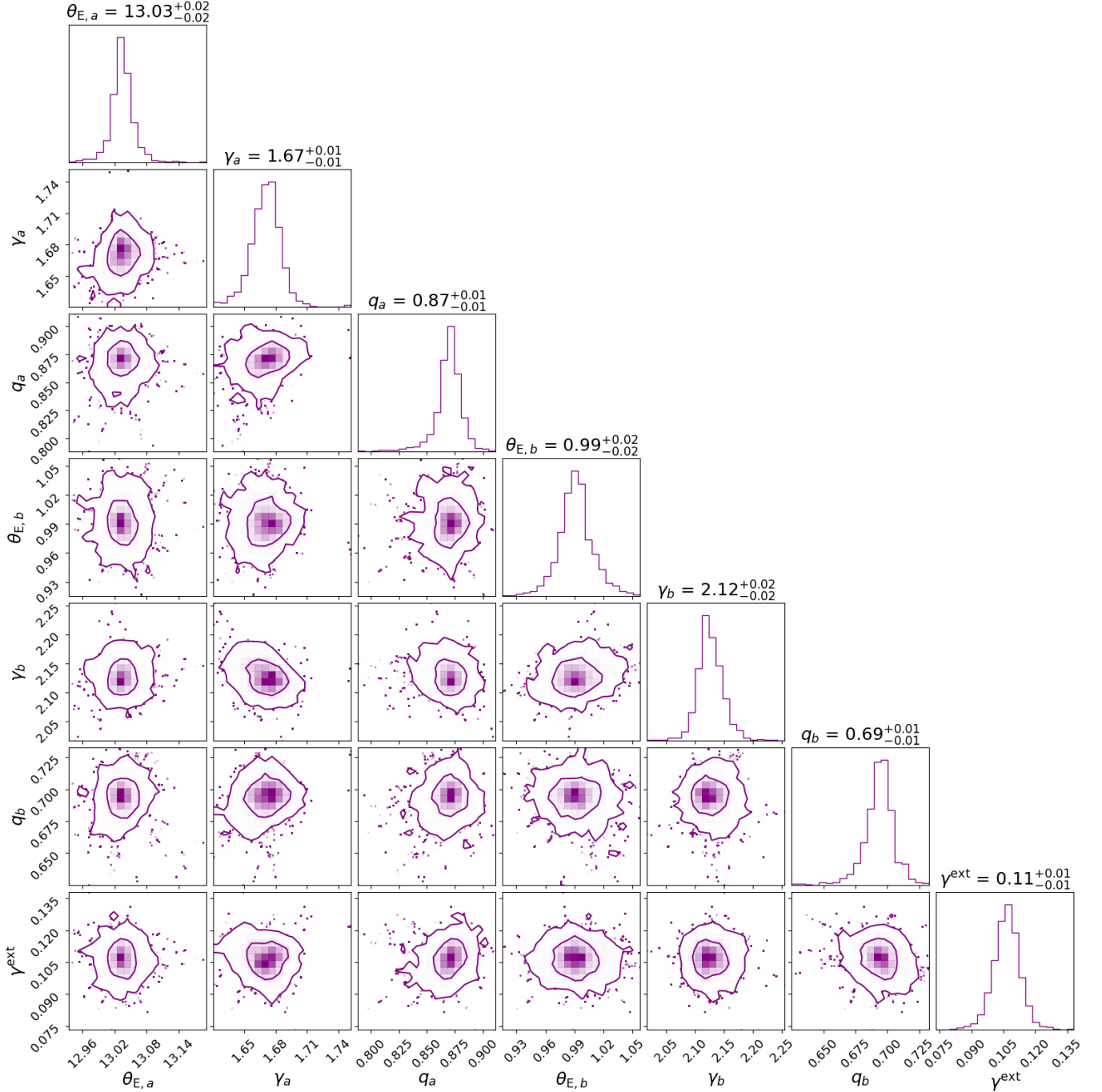
Figure 5. Posteriors of our lens model parameters. Also see Table 2 for a description and summary of each parameter values, as well as the angular configuration components to the lens profiles (i.e., PA_a, PA_b, and ϕ^{ext}). The inner and outer contours in the 2D distributions represent 68th and 95th percentiles, respectively.

the density profile slope of a cluster-scale halo is expected to vary. In this work, we do not account for this possible systematic effect (of a radius-dependent γ) as this would require a significantly more complex model, which we discuss later. Hence we only present the statistical uncertainties associated with our lens model. The best-fit γ we present can be seen as an average logarithmic power-law slope at different Einstein radii (with $z_s = 0.962, 1.166$, and 1.432).

Despite using a relatively simple lens model, we are able to adequately model DESI-090.9854-35.9683. This is likely due to the fact that DESI-090.9854-35.9683 is relaxed and therefore well-approximated as a power law within
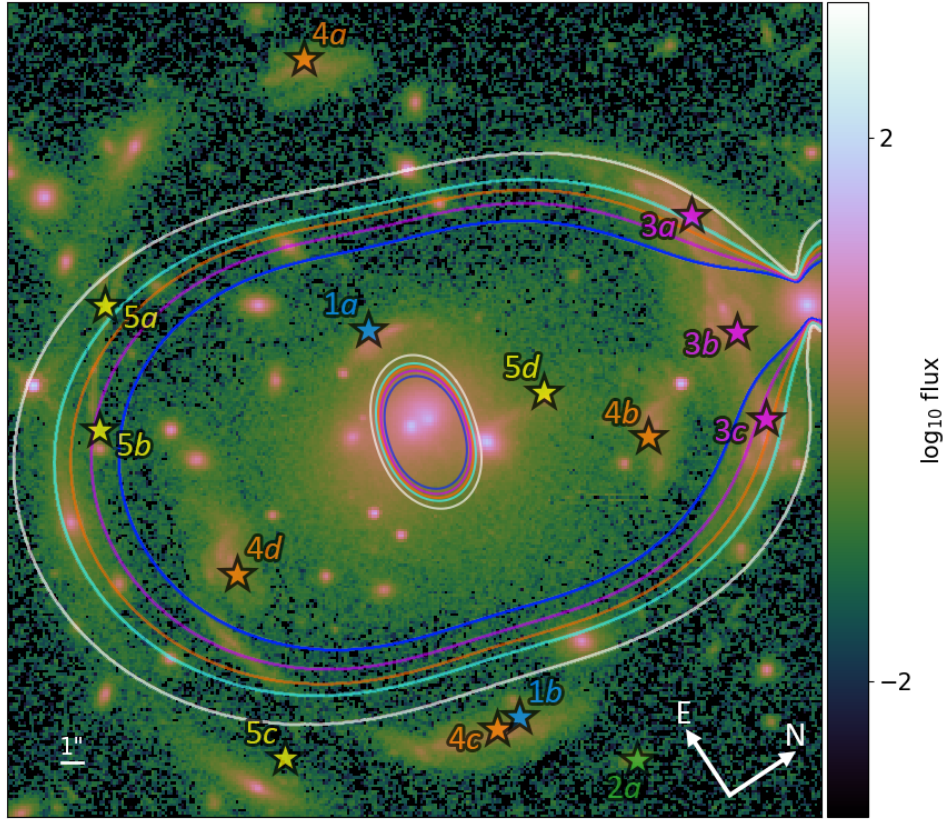
Figure 6. Predicted image locations and critical curves (blue, purple, orange, cyan, and white for $z_s = 0.962, 1.166, 1.432, 1.75,$ and 4.52, respectively) of our model, plotted over the *HST* F140W image. We use the centers of the shapelets source light profiles as the source image position on their respective source plane, for source galaxies 1, 3, 4, and 5. We use the Sérsic source light profile center for source galaxy 2, as we do not model for an additional shapelets basis.

the Einstein radii regime. However, future high-resolution X-ray, additional high resolution imaging, and/or deeper spectroscopic observations may warrant increasing the lens model complexity.

5. INFERRING THE REDSHIFT OF SOURCE GALAXY 7

Though we do not have spectroscopic redshift confirmation of source galaxy 7, we can estimate its redshift by extrapolating our lens model. In our model, the only quantities that change with source redshift are the Einstein radii,

$$\theta_E \propto \sqrt{\frac{D_{ls}}{D_s}}, \tag{1}$$

where D_{ls} is the angular diameter distance between the lens and source, and D_s is the angular diameter distance to the source. We can then simply use our best-fit lens model, fix all parameters except the Einstein radii of our two lens potentials (while fixing the ratio between the two), and fit for the source galaxy position that best reproduces the image positions and flux ratios of $7a$, $7b$, and $7c$. From the best-fitting θ_E, we can estimate the source redshift by assuming a standard flat ΛCDM cosmology of $H_0 = 70$ km s^{-1} Mpc^{-1} and $\Omega_M = 0.3$.

The *HST* F140W observed magnitudes are shown in Table 3. The image locations are assumed to have generous uncertainties of $\pm 0.5''$, to account for possible systematic uncertainty within our model. From these quantities, we fit for the source galaxy position and source redshift that maximizes the log-likelihood of the lensed positions and normalized fluxes of images $7a$, $7b$, and $7c$.

Using this scheme, we estimate source galaxy 7 has a redshift of $z_s = 4.52^{+1.03}_{-0.71}$, and magnifications of $8.56^{+0.20}_{-0.19}$, $12.86^{+0.36}_{-0.34}$, $9.73^{+0.26}_{-0.25}$ at $7a$, $7b$, and $7c$, respectively. While we do not include image $7d$ in our calculation (since its location and flux are not as well defined as the other images), our best-fitting results predict a radial arc within $\sim 1''$

Table 3. AB apparent magnitudes of images 7a, 7b, and 7c in various bands. The first three rows are obtained using a 1.4″ diameter aperture photometry. The last row uses a larger elliptical aperture photometry (3.7× more area) as to capture most of the object's flux; this is only applied onto image 7b as there are neighboring galaxies near 7a and c that would significantly skew the flux measurements. The band's effective wavelength is given below the band name.

Object	DECam g	F200LP	DECam r	DECam i	DECam z	VISTA J	F140W	VISTA Ks
	4730 Å	4970 Å	6420 Å	7840 Å	9260 Å	12500 Å	13920 Å	21500 Å
7a	$25.1^{+0.6}_{-0.4}$	$25.5^{+0.4}_{-0.3}$	$23.7^{+0.2}_{-0.1}$	$22.5^{+0.1}_{-0.1}$	$21.9^{+0.1}_{-0.1}$	$23.1^{+0.4}_{-0.3}$	$21.35^{+0.01}_{-0.01}$	$21.5^{+0.5}_{-0.3}$
7b	$25.2^{+0.7}_{-0.4}$	$25.1^{+0.2}_{-0.2}$	$23.1^{+0.1}_{-0.1}$	$22.3^{+0.1}_{-0.1}$	$21.6^{+0.1}_{-0.1}$	$22.2^{+0.1}_{-0.1}$	$21.15^{+0.01}_{-0.01}$	$21.1^{+0.3}_{-0.2}$
7c	$24.8^{+0.4}_{-0.3}$	$25.7^{+0.5}_{-0.3}$	$23.6^{+0.2}_{-0.1}$	$22.6^{+0.1}_{-0.1}$	$21.8^{+0.1}_{-0.1}$	$22.4^{+0.2}_{-0.2}$	$21.24^{+0.01}_{-0.01}$	$21.2^{+0.4}_{-0.3}$
7b	$24.0^{+0.4}_{-0.3}$	$24.8^{+0.6}_{-0.4}$	$22.3^{+0.1}_{-0.1}$	$21.3^{+0.1}_{-0.1}$	$20.7^{+0.1}_{-0.1}$	$21.3^{+0.1}_{-0.1}$	$20.51^{+0.01}_{-0.01}$	$20.3^{+0.2}_{-0.1}$

of 7d. We reiterate that systematic effects are not accounted for within our models; this estimate assumes a constant γ for the modeled perturbers and the uncertainty is purely statistical (see §4). Assuming this redshift, it should be possible to detect Lyman-α emission within the MUSE data, but we do not detect any prominent lines, possibly due to its absence or the low signal-to-noise of source galaxy 7 in the MUSE data.

One possibility is that the Mg II emission line doublet ($\lambda\lambda$ 2796 and 2803; typically prominent in the broad-line region of AGNs) may contribute to the F140W flux at that redshift, and could partially justify its brightness. The general trend in the SED identified from our photometry seem qualitatively similar to the NIRSpec/PRISM spectra of MSAID45924 (Greene et al. 2023), a $z = 4.46$ AGN identified by the *James Webb Space Telescope* (*JWST*), though it does not have prominent Mg II emission. However, given we do not observed a point source in any of the images, we find this conclusion unlikely. Another possibility is that this is a high-redshift quiescent galaxy, due to its red color across $5000 - 21000$ Å (see Table 3). *HST* has identified similar red, quiescent galaxies up to $z = 4$ (e.g., Glazebrook et al. 2017; Schreiber et al. 2018), and *JWST* up to $z = 5$ (e.g., Carnall et al. 2023; Setton et al. 2024; de Graaff et al. 2024). This theory is supported by the fact that while we faintly observe a continuum for source 7 in the MUSE data, we do not observe any identifiable emission lines, which could indicate quiescence. If this is the case, source galaxy 7 could serve as additional evidence for early galaxy quenching more efficiently than previously understood. With deeper spectroscopy, we will be able to determine the identity and redshift of source galaxy 7 with more confidence.

We do not apply the same analysis on source 6 as we did for source 7 for two reasons. Firstly, we are not certain that the images 6a and 6b are indeed of the same source galaxy. Unlike with source 7, where it is visually obvious that 7a, b, and c belong to the same source (due to striking similarity in colors and a textbook orientation of its lensed images), this is not the case for source 6. Secondly, images 6a and 6b are much more diffused, complex, and crowded (hence much more difficult to accurately recover photometry for) compared to the compact images of 7a, b, and c. As the photometry is a necessary part of the analysis performed on source 7, this would make it much more difficult to accurately estimate a redshift for source 6. Instead, if we assume that images 6a and 6b are the same source, we can deduce that the outer critical curve should cross between the two images. From this, our model infers that the redshift of source 6 should lie between $1.75 \leq z_\mathrm{s} \leq 4.52$ (see the cyan and white contours of Figure 6).

6. DISCUSSION AND CONCLUSION

In this paper, we present DESI-090.9854-35.9683, a cluster-scale lens first identified in Jacobs et al. (2019), and later independently found in Huang et al. (2021) and O'Donnell et al. (2022). From *HST* observations in the F140W and F200LP bands (16773; K. Glazebrook), we identify seven possible lensed sources. With spatially resolved spectroscopic observations from MUSE, we confirm five of these lensed sources, and provide the proper velocities for the resolved images. From this, we construct a simple yet successful lens model using only two elliptical power law mass profiles and external shear. We use this model to infer that one of the spectroscopically unresolved sources (source galaxy 7) is at a redshift of $z_\mathrm{s} = 4.52^{+1.03}_{-0.71}$, while the other (source galaxy 6) is at a redshift range of $1.75 \leq z_\mathrm{s} \leq 4.52$.

In this spectacular system, nearly all the "classic" lensing configurations are represented. Arc family 2 is singly imaged, as its source is outside of the caustics. The source for arc family 1 is well inside the radial caustic but just outside the tangential (diamond) caustic, and thus is doubly lensed (though there ought to be a third, highly de-

magnified image near the lens center). Arc family 5 has a predicted fourth image matching an observed object, and forms a "fold" configuration. Whereas arc family 3 has three images, exhibiting a "naked cusp" configuration. Arc family 4 forms a quintessential Einstein cross. Finally, arc family 7 appears to have four images, including a possible radial arc, and if confirmed, this would form a "cusp" configuration (likely, also a naked cusp; see Figure 2 of Lewis et al. 2002).

With additional spectroscopic observations to confirm source galaxies 6 and 7, deeper X-ray observations to better constrain the gaseous intracluster medium of this system (e.g., Caminha et al. 2016; Mahler et al. 2023), and/or deeper higher-resolution imaging, we can construct an even more accurate model of this system with fewer assumptions of the total mass profile. In addition to the potential systemic effect of γ varying with cluster-centric radius (see §4), another possible systematic effect that a more comprehensive lens model may need to take into account is the gravitational effects of the nearby sources on sources that are further away (i.e., not just multiple source planes, but also multiple lens planes). It then becomes possible to constrain cosmological parameters such as Ω_M and w (e.g., Collett & Auger 2014). Furthermore, the large number of lensed sources can translate to tighter constraints on the matter profile of the lens galaxy, allowing for closer examination of the dark matter and luminous matter distributions/interactions in galaxy clusters.

Clearly, there is much more to be learned from this system. The coincidental alignment of seven galaxies and a foreground galaxy cluster can give us unprecedented insight into the universe, whether it be high redshift galaxies, cluster properties, or cosmology.

REFERENCES

Astropy Collaboration, Robitaille, T. P., Tollerud, E. J., et al. 2013, A&A, 558, A33, doi: 10.1051/0004-6361/201322068

Astropy Collaboration, Price-Whelan, A. M., Sipőcz, B. M., et al. 2018, AJ, 156, 123, doi: 10.3847/1538-3881/aabc4f

Astropy Collaboration, Price-Whelan, A. M., Lim, P. L., et al. 2022, ApJ, 935, 167, doi: 10.3847/1538-4357/ac7c74

Bacon, R., Accardo, M., Adjali, L., et al. 2010, in Ground-based and Airborne Instrumentation for Astronomy III, ed. I. S. McLean, S. K. Ramsay, & H. Takami (SPIE), doi: 10.1117/12.856027

Birrer, S., & Amara, A. 2018, Physics of the Dark Universe, 22, 189, doi: 10.1016/j.dark.2018.11.002

Birrer, S., Amara, A., & Refregier, A. 2015, ApJ, 813, 102, doi: 10.1088/0004-637X/813/2/102

Birrer, S., Shajib, A., Gilman, D., et al. 2021, The Journal of Open Source Software, 6, 3283, doi: 10.21105/joss.03283

Bradač, M., Schneider, P., Lombardi, M., et al. 2004, Astronomy & Astrophysics, 423, 797–809, doi: 10.1051/0004-6361:20040168

Caminha, G. B., Grillo, C., Rosati, P., et al. 2016, Astronomy & Astrophysics, 587, A80, doi: 10.1051/0004-6361/201527670

Carnall, A. C., McLure, R. J., Dunlop, J. S., et al. 2023, Nature, 619, 716–719, doi: 10.1038/s41586-023-06158-6

Collett, T. E., & Auger, M. W. 2014, MNRAS, 443, 969, doi: 10.1093/mnras/stu1190

de Graaff, A., Setton, D. J., Brammer, G., et al. 2024, Efficient formation of a massive quiescent galaxy at redshift 4.9. https://arxiv.org/abs/2404.05683

Ding, X., Treu, T., Birrer, S., et al. 2021, Monthly Notices of the Royal Astronomical Society, 503, 1096, doi: 10.1093/mnras/stab484

Flesch, E. 2010, Publications of the Astronomical Society of Australia, 27, 283–289, doi: 10.1071/as09060

Foreman-Mackey, D., Hogg, D. W., Lang, D., & Goodman, J. 2013, Publications of the Astronomical Society of the Pacific, 125, 306–312, doi: 10.1086/670067

Glazebrook, K., Schreiber, C., Labbé, I., et al. 2017, Nature, 544, 71, doi: 10.1038/nature21680

Greene, J. E., Labbe, I., Goulding, A. D., et al. 2023, arXiv e-prints, arXiv:2309.05714, doi: 10.48550/arXiv.2309.05714

Harris, C. R., Millman, K. J., van der Walt, S. J., et al. 2020, Nature, 585, 357, doi: 10.1038/s41586-020-2649-2

Hilton, M., Sifón, C., Naess, S., et al. 2021, The Astrophysical Journal Supplement Series, 253, 3, doi: 10.3847/1538-4365/abd023

Huang, X., Storfer, C., Gu, A., et al. 2021, The Astrophysical Journal, 909, 27, doi: 10.3847/1538-4357/abd62b

Hunter, J. D. 2007, Computing in Science & Engineering, 9, 90, doi: 10.1109/MCSE.2007.55

Jacobs, C., Collett, T., Glazebrook, K., et al. 2019, The Astrophysical Journal Supplement, 243, 17, doi: 10.3847/1538-4365/ab26b6

Kluyver, T., Ragan-Kelley, B., Pérez, F., et al. 2016, in Positioning and Power in Academic Publishing: Players, Agents and Agendas, ed. F. Loizides & B. Schmidt, IOS Press, 87 – 90

Kochanek, C. S. 1992, ApJ, 384, 1, doi: 10.1086/170845

Lewis, G. F., Carilli, C., Papadopoulos, P., & Ivison, R. J. 2002, Monthly Notices of the Royal Astronomical Society, 330, L15–L18, doi: 10.1046/j.1365-8711.2002.05260.x

Mahler, G., Jauzac, M., Richard, J., et al. 2023, ApJ, 945, 49, doi: 10.3847/1538-4357/acaea9

Mostoghiu, R., Knebe, A., Cui, W., et al. 2019, MNRAS, 483, 3390, doi: 10.1093/mnras/sty3306

Narayan, R., & Wallington, S. 1992, in Gravitational Lenses, ed. R. Kayser, T. Schramm, & L. Nieser (Berlin, Heidelberg: Springer Berlin Heidelberg), 12–26

Navarro, J. F., Frenk, C. S., & White, S. D. M. 1996, ApJ, 462, 563, doi: 10.1086/177173

Newman, A. B., Treu, T., Ellis, R. S., et al. 2013, The Astrophysical Journal, 765, 24, doi: 10.1088/0004-637x/765/1/24

Nightingale, J. W., Dye, S., & Massey, R. J. 2018, Monthly Notices of the Royal Astronomical Society, 478, 4738, doi: 10.1093/mnras/sty1264

O'Donnell, J. H., Wilkinson, R. D., Diehl, H. T., et al. 2022, ApJS, 259, 27, doi: 10.3847/1538-4365/ac470b

Refregier, A. 2003, Monthly Notices of the Royal Astronomical Society, 338, 35–47, doi: 10.1046/j.1365-8711.2003.05901.x

Refregier, A., & Bacon, D. 2003, Monthly Notices of the Royal Astronomical Society, 338, 48–56, doi: 10.1046/j.1365-8711.2003.05902.x

Roberts-Borsani, G., Morishita, T., Treu, T., et al. 2022, ApJL, 938, L13, doi: 10.3847/2041-8213/ac8e6e

Schreiber, C., Labbé, I., Glazebrook, K., et al. 2018, Astronomy & Astrophysics, 611, A22, doi: 10.1051/0004-6361/201731917

Sérsic, J. L. 1963, Boletin de la Asociacion Argentina de Astronomia La Plata Argentina, 6, 41

Setton, D. J., Khullar, G., Miller, T. B., et al. 2024, UNCOVER NIRSpec/PRISM Spectroscopy Unveils Evidence of Early Core Formation in a Massive, Centrally Dusty Quiescent Galaxy at $z_{spec} = 3.97$. https://arxiv.org/abs/2402.05664

Shajib, A. J., Treu, T., Birrer, S., & Sonnenfeld, A. 2021, MNRAS, 503, 2380, doi: 10.1093/mnras/stab536

Shajib, A. J., Birrer, S., Treu, T., et al. 2018, Monthly Notices of the Royal Astronomical Society, 483, 5649, doi: 10.1093/mnras/sty3397

Soto, K. T., Lilly, S. J., Bacon, R., Richard, J., & Conseil, S. 2016, MNRAS, 458, 3210, doi: 10.1093/mnras/stw474

Tan, C. Y., Shajib, A. J., Birrer, S., et al. 2024, Monthly Notices of the Royal Astronomical Society, 530, 1474–1505, doi: 10.1093/mnras/stae884

Tarrío, P., Melin, J.-B., & Arnaud, M. 2019, Astronomy & Astrophysics, 626, A7, doi: 10.1051/0004-6361/201834979

Virtanen, P., Gommers, R., Oliphant, T. E., et al. 2020, Nature Methods, 17, 261, doi: 10.1038/s41592-019-0686-2

Voges, W., Aschenbach, B., Boller, T., et al. 2000, VizieR Online Data Catalog: ROSAT All-Sky Survey Faint Source Catalog (Voges+ 2000), VizieR On-line Data Catalog: IX/29. Originally published in: 2000IAUC.7432R...1V

Weilbacher, P. M., Palsa, R., Streicher, O., et al. 2020, A&A, 641, A28, doi: 10.1051/0004-6361/202037855

Wong, K. C., Suyu, S. H., Chen, G. C. F., et al. 2020, MNRAS, 498, 1420, doi: 10.1093/mnras/stz3094